Designing Anisotropic Friction through Limit Curve Analysis

by

Elizabeth Danielle Vasquez

Submitted to the

Department of Mechanical Engineering

in Partial Fulfillment of the Requirements for the Degree of

Bachelor of Science in Mechanical Engineering

at the

Massachusetts Institute of Technology

June 2019

Signature of Author: Signature redacted

Department of Mechanical Engineering

May 17, 2014

Certified by: Signature redacted

Alberto Rodriguez

Associate Professor in Mechanical Engineering

Thesis Supervisor

Signature redacted

Accepted by: _____

Maria Yang

Professor of Mechanical Engineering

Undergraduate Officer

Designing Anisotropic Friction through Limit Curve Analysis

by

Elizabeth Danielle Vasquez

Submitted to the Department of Mechanical Engineering

on May 17, 2019 in Partial Fulfillment of the

Requirements for the Degree of

Bachelor of Science in Mechanical Engineering

ABSTRACT

Friction is an essential component of robotic manipulation which is highly dependent on contact surfaces. In practical applications, these surfaces are often anisotropic, a property that has been known to produce interesting movements in nature and uncertainty in human applications. Therefore, control of anisotropic frictional surfaces could result in more precise movement in manipulation, locomotion, and other facets touched by frictional contact. To arrive at such controllability, frictional force was collected across a spectrum of anisotropic micro-textures, and a limit curve was generated. Experimental data was analyzed in accordance to friction laws such as limit curve and maximum-inequality principle (MPI). Qualitative observation and residual sum of squares (RSS) was used to detect lack of normality and non-convexity within each limit curve. This lack of both normality and convexity contradicts MPI and suggests that an alternative model is necessary. Additionally, the anisotropic frictional behaviors observed advances the feasibility of "designing" micro-textures capable of controllable anisotropic friction.

Thesis Supervisor: Alberto Rodriguez

Tile: Associate Professor in Mechanical Engineering

Acknowledgments

The author would like to thank Dr. Kevin Cedrone and Dr. Barbara Hughey for their guidance in analyzing the data, Kurt Broderick and the MIT Microsystems Technology Laboratories for their assistance and expertise in photolithography wafer fabrication, the MIT Center for Materials Science and Engineering (CMSE) for use of their Scanning Electron Microscope, and the entire Manipulation and Mechanisms Laboratory (MCube) at MIT – especially Professor Alberto Rodriguez - for their support and guidance. The author also would like to give special thanks to Dr. Daolin Ma for his constant guidance throughout the entire project.

Table of Contents

List of Figures

List of Tables

1. Introduction

A strong understanding of frictional forces is critical to almost all forms of robotic manipulation and locomotion. Often times, this friction between robotic surfaces is anisotropic and spatially distributed which complicates and can produce variability in trajectories [1] [2]. Currently there exists different methods of modeling friction in robotic and non-robotic interactions from data-driven to analytical models [2][3][4][5], but there is great opportunity in not only understanding and accounting for but also controlling frictional interactions. This has long been exploited by nature in the micro-textures of animal surfaces. Take the undulating locomotion of a snake for example, whose skin produces direction-dependent coefficients of friction to achieve more efficient forward propulsion [6].

Beyond the benefits afforded to nature through friction control, the lack of such control in robotics research has produced uncertainties which demonstrates the relevance and need for friction control in robotics. For example, an experiment in which a robotic arm pushed an object back and forth in a consistent way multiple times resulted in a significant disparity in each trajectory [2]. This uncertainty in trajectory was found to be caused mostly by the specific anisotropic properties of the contact surface which explained the stochasticity in the outcome of a push, i.e. a lack of control over frictional contact forces resulted in uncertainty in pushes. Further, anisotropic friction has been found to lead to certain convergence behaviors [7]. Hence there is a clear need and opportunity for control of these anisotropic responses.

In the aforementioned experiment and many others, better control over the frictional contact forces could lead to guaranteed convergence of motion in robotics. By understanding how directional and spatial patterns of micro-textures affect frictional properties - taking a cue from nature - one could potentially control friction to produce favorable directional behaviors thus giving robots more precise physical interactions with their environment.

Therefore, it is of interest to determine if it is possible to design contact surfaces with micro-textures that allow for the quantified control of contact forces such that motion can be guided toward desired trajectories or motions. Ultimately, the goal of this work is to generate a map of micro-textures for a desired friction map. However, the first steps which were carried out were to collect data - frictional force - to better understand and model anisotropic friction. This data was collected via controlled experiments on samples with specifically designed micro-textures. Photolithography and molding techniques – widely used in MEMS development- were utilized to produce the desired micro-textures on the samples. The following chapters discuss the fabrication, data acquisition, and analysis of this exploratory research via limit curves and residual sum of squares (RSS) with the goal of understanding anisotropic friction for the purposes of improved control of frictional interactions.

2. Background

2.1 Limit Curve

A limit curve is a way to visualize frictional properties in a compact way. As shown in Figure 1, a limit curve and the space inside the limit curve in regard to friction identifies every frictional force possible for a given point contact instance.

In the case of isotropic, Coulombic friction, the friction force is of a constant magnitude which is opposite of the slip direction therefore the limit curve will be a circle. In the case of anisotropic friction, the shape can be very different but usually a similar convexity is expected; for example the shape is naturally expected to resemble an ellipse [8].

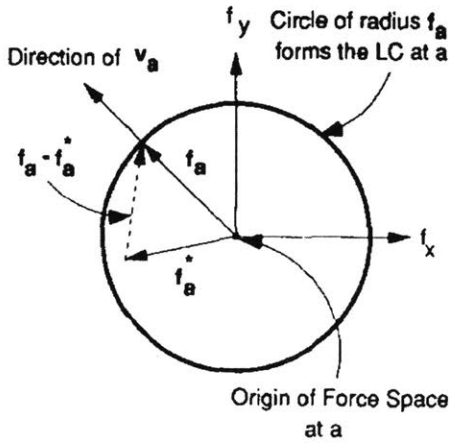

Figure 1: Illustrated is the limit curve for an isotropic, point-contact friction interaction whereby the circle represents the maximum friction force possible in a given contact interaction. The slip velocity v_a points normal to the limit curve. Any force within the curve is representative of static friction, and a force on the curve represents dynamic friction. Figure from [9].

2.2 Maximum Power Inequality Principle (MPI)

The maximum-power inequality (MPI), also known as the maximum plastic work, is as follows:

$$(f - f^*)v \geq 0$$

where f is the actual friction force and v is the actual slip velocity at the point of contact. The idea behind this is that one should seek to maximize the total power over all arbitrary f^* such that f and f^* are within or on the limit curve derived, given that the limit curve and the slip velocity are known. A straightforward interpretation of MPI is that the sliding velocity corresponding to a force on limit curve is perpendicular to the curve at that point. MPI is simply a way to determine the corresponding force associated with a slip velocity, and the implication is normality.

In order to construct a limit curve, this principle must be enforced; and it ensures that the resulting limit curve will be convex [9].

Interpreting the limit curve and applying MPI some key take-aways are as follows:

(a) The slip velocity is zero if the actual force is inside the limit curve
(b) The slip velocity is perpendicular to the limit curve when a well-defined normal exists, known as satisfying normality.
(c) The slip direction is non-unique if the friction force is at a vertex in the limit curve [9]

These assumptions and principles will be further discussed in the analysis of anisotropic friction.

3. Experimental Design

3.1 Procedural Overview

In order to create various micro-textures, a film photomask was created for each specific micro-texture. This mask was then used in a photolithographic process to fabricate the anisotropic textures on a silicon wafer. A soft mold was created from the wafer, and the sample – upon which experimental data was derived - was then cast out of the softer mold. Figure 2 shows the actual wafer, soft mold, and sample. For each sample, a glass ball was run across the micro-texture at varying slip velocities, constant magnitude (40 mm/s) varying directions. These results were recorded and plotted on a limit curve. The RSS values of each limit curve were computed to analytically demonstrate non-convexity.

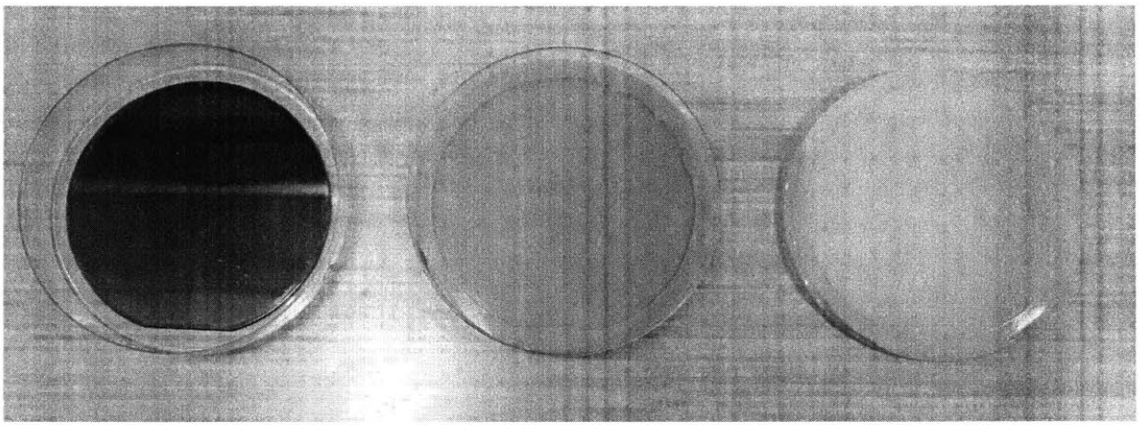

Figure 2: Left most object is a fabricated silicon wafer upon which the middle object – the softer mold – is molded on. The right most object is the sample upon which experimental data is procured. The sample was cast from the middle, softer mold.

3.2 Sample Fabrication

3.2.1 Texture Design

In order to explore different anisotropic micro-textures, valleys and canyons were employed, whereby the width of the valleys, d_1, and canyons, d_2, were varied with each distinct micro-texture. See Figure 3. This grooved texture is commonly utilized to explore anisotropic friction [10][11][12]. Additionally it has been shown that varying the number of grooves could be a mechanism of controlling friction [12].Therefore this grooved pattern was explored further on the micron scale where the texture can still be expected to produce a similar non-trivial frictional behavior without being visually seen or felt. Given the constraints of the fabrication method, described in detail in a subsequent section, a three-by-three matrix of d_1 and d_2 values were initially defined for three different materials (TASK™16, Smooth-Cast® 61D, and PMC®-770). See Figure 4 for initial testing matrix. From these results, a single material was selected, and the matrix was expanded to a six-by-six matrix, as shown in Figure 5. It should be noted that originally, a single sample had only one micro-texture, but as the study progressed it was noted that multiple textures, i.e. four textures, could be etched into a single silicon wafer. Therefore, some samples contain only one micro-texture and others contain four.

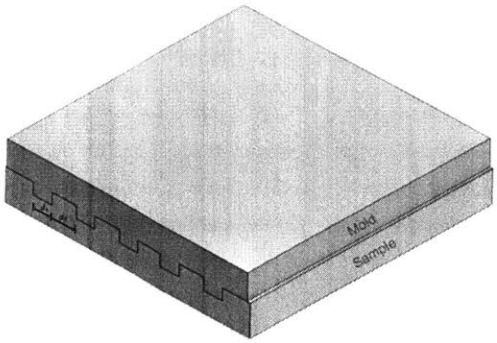

Figure 3: Diagram of the definition of micro-textures dimensions. Each micro-texture was composed of a series of valleys and canyons. The exact width of the valley and canyon was changed for each individual sample. The width of the valley is defined as d_1, and the width of the canyon is defined as d_2. The upper layer of the diagram labeled "Mold" refers to the first mold, molded from the silicon wafer, and the bottom layer labeled "Sample" refers to the actual sample upon which frictional force data was experimentally obtained.

	d_1		
d_2	24 μm	48 μm	72 μm
24 μm	A1	A2	A3
48 μm	A4	A5	A6
72 μm	A7	A8	A9

Figure 4: The initial sample parameter matrix whereby values of d_2 correspond to the rows and values of d_1 correspond to the columns. Each cell represents a sample to be fabricated with the corresponding d_1 and d_2 values. The content in each cell (A1, A2, etc.) is the reference value for that sample which is used to identify each sample. This sample parameter matrix was utilized to create the nine initial micro-textures for each of the three materials tested: 61D, PMC, and TASK16.

d_2	d_1 12 µm	24 µm	48 µm	60 µm	72 µm	90 µm
12 µm	B1	B2	B3	B4	B5	B6
24 µm	B7	B8	B9	B10	B11	B12
48 µm	B13	B14	B15	B16	B17	B18
60 µm	B19	B20	B21	B22	B23	B24
72 µm	B25	B26	B27	B28	B29	B30
90 µm	B31	B32	B33	B34	B35	B36

Figure 5: The final TASK16 six-by-six sample parameter matrix whereby values of d_2 correspond to the rows and values of d_1 correspond to the columns. Each cell represents a sample to be fabricated with the corresponding d_1 and d_2 values. The content in each cell (B1, B2, etc.) is the reference value for that sample which is used to identify each sample. This sample parameter matrix was utilized to create and reference the expanded micro-texture samples of TASK16.

3.2.2 Mask Printing

In order to physically create the 3D micro-textured samples, the first step was to create a 2D version of these micro-textures on AutoCAD. These files were then sent to a third-party provider, FineLine Imaging, to produce a laser film photomasks Figure 6.

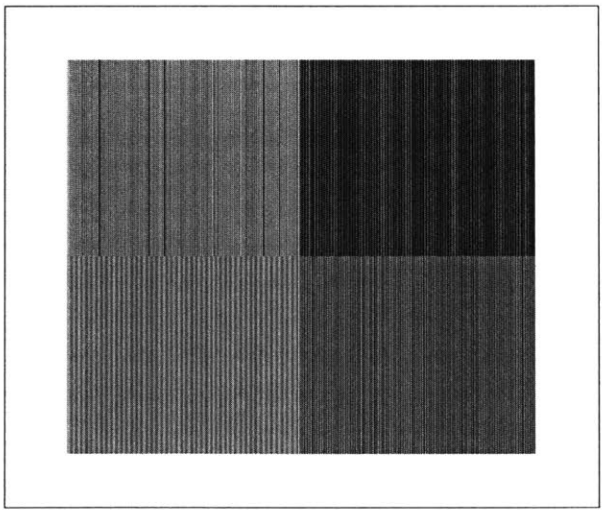

Figure 6: Pictured above is a film photomask for a single wafer with four different micro-textures used to produce a single sample.

3.2.3 Silicon Wafer Fabrication

Photolithography was used to etch the micro-texture from the mask into a four-inch silicon wafer. Specifically, SU-8 2025 was used to etch the micro-texture into the wafer, but a thin layer of SU-8 2005 was initially applied and exposed to ensure optimal adhesion of the thicker layer of SU-8 2025 on the wafer. Following the processing guidelines found on the MicroChem website, a feature thickness of 36 microns was achieved. The fabrication process for a silicon wafer was as follows: dehydrate wafer, spin coat SU-8 2005, soft bake, expose wafer without mask, post exposure bake, spin coat SU-8 2025, soft bake, post exposure bake, develop, expose wafer to a desiccator controlled environment with approximately a milliliter of either Tricholorosilane or Octotrichloride. The final step utilizing the desiccator is employed to prevent adhesion of molding material to silicon wafer during the molding process. Figure 7 pictorially describes this process, and Figure 8 depicts fabricated wafer.

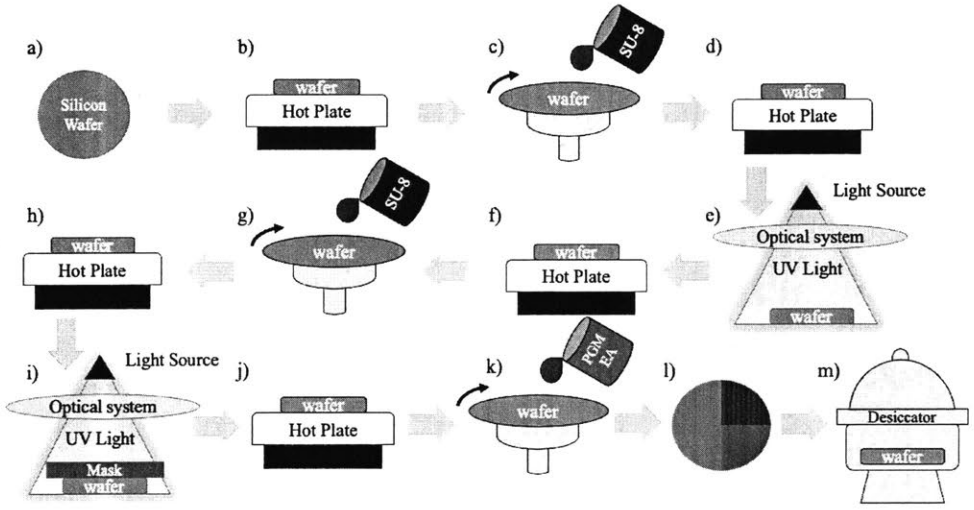

Figure 7: Diagram illustrates the photolithography process used to fabricate a silicon wafer with micro-textures. From step a) to b) an unused silicon wafer is heated on a hot plate to dehydrate it. In c) SU-8 2005 is spin coated onto the wafer. In d) the wafer is soft baked to promote adhesion and remove solvents from the SU-8. In e) the wafer is exposed to UV light without a mask to serve as a base layer for the next layer of SU-8 2025 to stick. In f) the wafer undergoes post exposure baking, in g) SU-8 2025 is spin coated, in h) the wafer is soft baked, in i) the wafer is exposed again but this time with the mask containing the desired micro-texture, in j) the wafer undergoes post exposure baking, in k) the wafer is developed using Propylene glycol methyl ether acetate (PGMEA), in l) the wafer now has the desired micro-textures, and in m) the wafer is placed in a desiccator for thirty minutes with a milliliter of either Tricholorosilane or Octotrichloride.

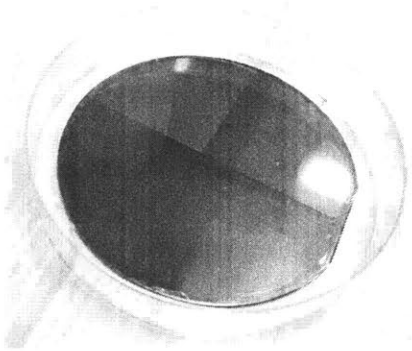

Figure 8: Finished four-inch, silicon wafer with four micro-textures etched into the surface via photolithography.

3.2.4 Sample Molding

After a silicon wafer with the desired micro-texture/textures had been fabricated, the wafer was used to produce a mold composed of a soft silicone rubber (Mold Star™ 15 SLOW) shown in Figure 9. This is the layer defined as "Mold" in Figure 2. Mold Star™ 15 SLOW was selected as the first mold due to its compliance which makes it easier to remove from the wafer without damage. This softer mold was then used to create a cast out of a harder rubber (TASK™16, Smooth-Cast® 61D, and PMC®-770). The resulting cast was the sample which was tested in the experimental setup to yield frictional data.

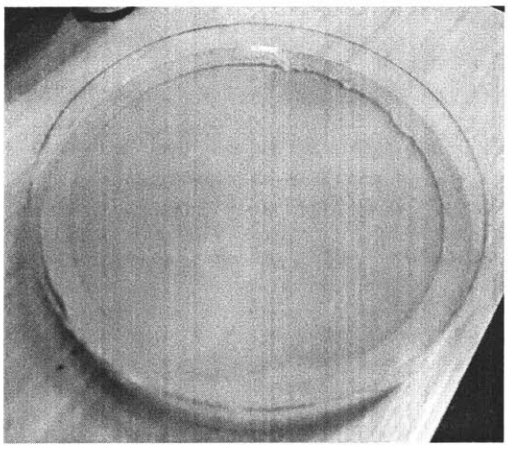

Figure 9: Mold Star™ 15 SLOW molded directly from a fabricated silicon wafer with four micro-textures on it. The samples made from the three harder rubbers (TASK™16, Smooth-Cast® 61D, and PMC®-770) were cast on top of this mold.

In order to fabricate the soft silicone mold, double-sided tape was used to adhere the silicon wafer to a five-inch Petri dish; and Mold Star™ 15 SLOW was poured onto the wafer inside the petri-dish which was degassed twice (once within the mixing cup and a second time inside the petri dish).

After the Mold Star™ 15 SLOW had cured, the mold was removed and taped to a new petri dish, and the general procedure above was repeated. Given the low stiffness of the mold, hot-glue was applied to most of the interface between the mold and the petri dish to prevent the edges of the mold from rising during the degassing process. A portion of the interface on opposite sides of each other was left unglued for air between the mold and the petri dish to be pulled out under vacuum.

Each micro-texture defined in the Figure 4 was created in each of the three rubbers (TASK™16, Smooth-Cast® 61D, and PMC®-770), and a blank sample, with no micro-textures, was also fabricated as a control. A picture of a fabricated TASK™16 sample is shown in Figure 10.

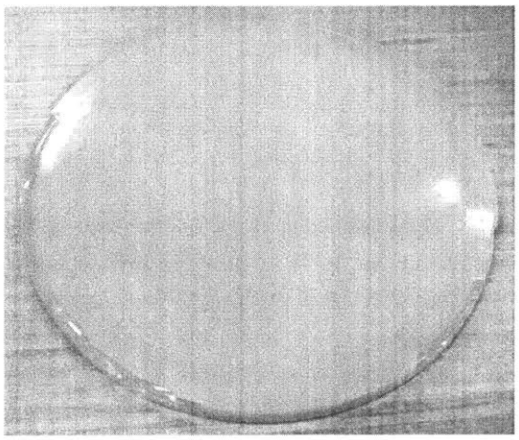

Figure 10: TASK16 sample with four micro-textures which was cast directly from the Mold Star™ 15 SLOW mold depicted in Figure 7. This is an example of the samples upon which frictional force measurements were extracted.

It should be noted that this fabrication technique could not produce complete uniformity between the valley and canyon width at all heights. Examining sample B8 (see Figure 5) under a MERLIN Field Emission Scanning Electron Microscope (FE-SEM), a taper in the canyon width along the feature's height and defects can be seen. See Figure 11 and 12 for imperfections and taper respectively. However, in spite of this, the overall micro-textures are relatively consistent and do contain the desired micro-textured pattern. Additionally, the defects exist on such a small scale that their effects are much smaller than the effects of the features on the sample when the entire micro-textured area is considered.

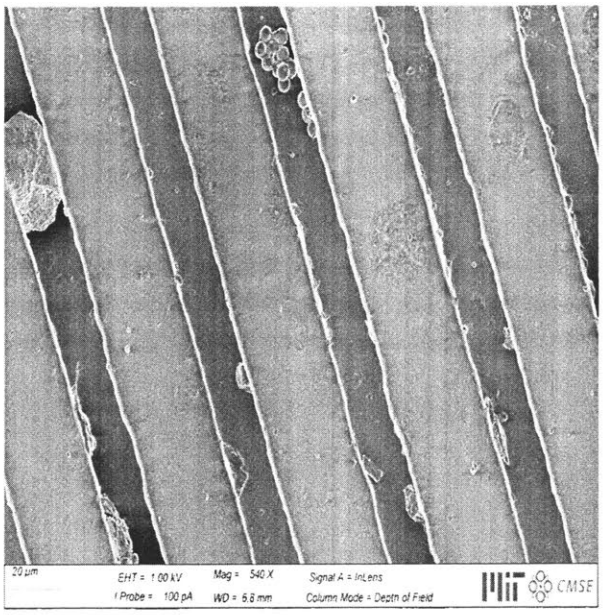

Figure 11: Top view of sample B8 under a 540x magnification using a MERLIN Field Emission Scanning Electron Microscope (FE-SEM). The micro-texture with valleys and canyons can be clearly seen across the sample. Defects can be seen clearly as aberrations in the pattern: splotches in the darker vertical portion of the picture.

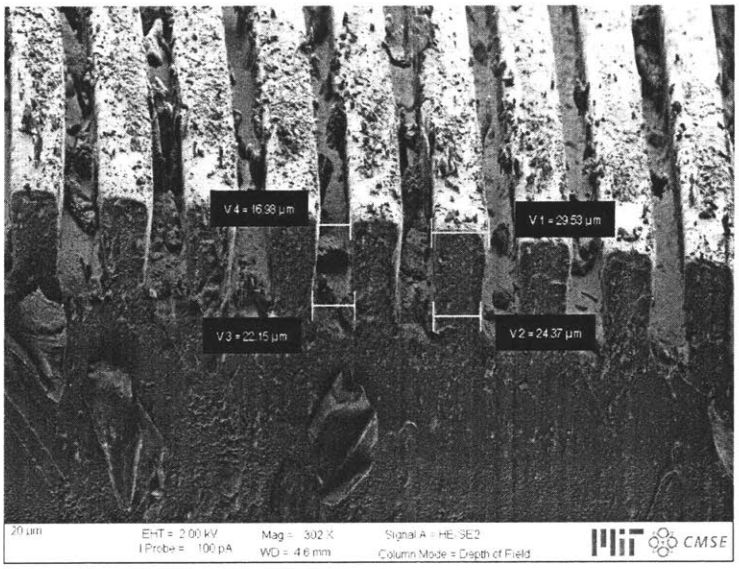

Figure 12: Angled view of sample B8 under 302x magnification using a MERLIN Field Emission Scanning Electron Microscope (FE-SEM). The base of the canyon feature appears to begin at approximately 24 μm and increases with the height of the feature. This is due to fabrication errors; however, a clear pattern of valleys and canyons of approximately the same width can be seen throughout the micro-texture. The particles that appear to coat the top edge of the surface are most likely due to the residue which adhered to the remaining features after the sample was cut and prepared for the FE-SEM.

3.3 Frictional Experimentation

3.3.1 Experimental Setup

The experimental setup consists of two Newmark linear stages [Speed Limit: 50 $\frac{mm}{s}$, Resolution: 0.1 μm, Accuracy: $\pm$ 3 μm] and one rotational stage – which was not utilized – that is controlled through a ROS network on Python. A ruby ball, which the sample is rubbed against, transmits the frictional force of contact through the aluminum bar to an ATI force/torque sensor: Gamma [Calibration: SI-32-2.5, Sensing Range: 32 N, Resolution: $\frac{1}{160}$ N]. The weight of the ruby ball and beam is balanced and accounted for such that a constant and known normal force can be applied to the point-contact force interaction. See Figure 13.

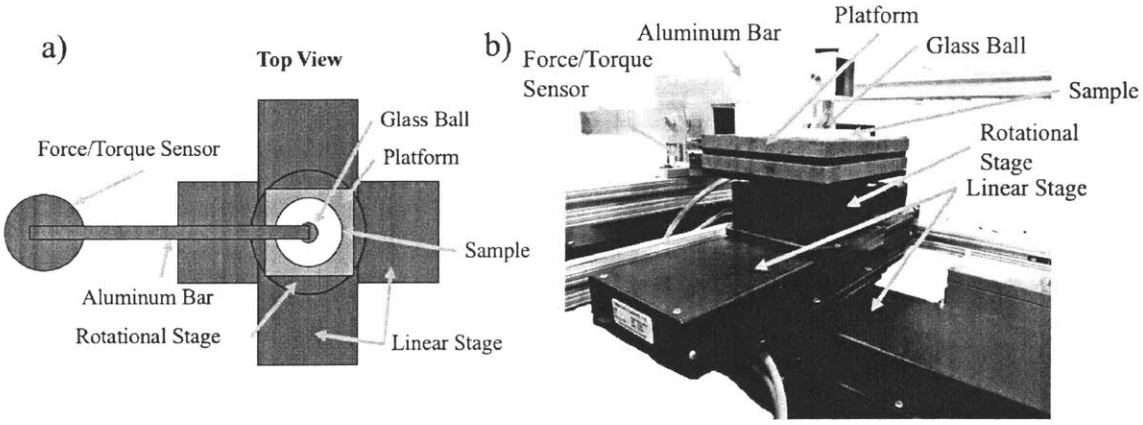

Figure 13: Diagrams illustrate the experimental setup. Figure a) is a top view, schematic of the experimental setup, and figure b) is an actual picture of the setup. During the experiment, the sample is centered on the platform and the operating program is initiated, which drives the encoders on the two linear stages to rub the micro-texture along various diameters of a circle centered on each micro-texture present on the sample. As the micro-texture is translated by the linear stages, the force of friction is transmitted through the glass ball and aluminum bar to the force/torque sensor where it is collected. Through this setup, the friction force for all trials was collected.

3.3.2 Testing Procedure

In order to collect frictional force measurements, the sample was centered on the platform. A hinge is present at the pivot point of the aluminum bar to allow for the glass ball to be lifted out of contact of the sample during sample placement. At the start of the experiment, a calibration is performed to adjust for the ambient forces felt when the glass ball is resting on the sample. A 207-gram weight is applied to a rod located on the same axis as the glass ball. The linear stages are then commanded to produce slip velocities along various diameters of a circle centered at the center of each micro-texture present on the sample. All code was written in Python utilizing ROS and the low-level control of the stages is performed in G-code with a Galil controller.

3.3.3 Data Analysis

To obtain the frictional coefficients in the x and y directions, the force obtained from the force/torque sensor is divided by a known normal force – produced by the added weight – to obtain the frictional coefficients. The slip velocity is also known based on the trajectories of the linear stages. With this information, a limit curve is constructed for each trial by physically plotting the frictional coefficient in x and y - depicted as a point - for a given slip velocity, depicted as a unit vector. See Figure 14 a) for an illustration of one of the limit curves obtained from a single trial of a single micro-texture on a single sample.

Given that an elliptical shape is the expected limit curve for an anisotropic micro-texture [8], it was valuable to quantify how non-elliptical each obtained limit curve was. A lack of convexity, symmetry, and normality in slip velocities would be seen as aberrations from the rules obtained from limit curve assumptions and MPI. Therefore, the data points in the limit curve were fit to an ellipse and the residual sum of squares (RSS) was found between the data and the best-fit-ellipse. See Figure 14 for depiction of best-fit-ellipse applied to the data points. Two trials of each micro-texture were conducted. RSS values for at least one trial were performed for all micro-textures. If the RSS value was found to be high or the limit curve looked qualitatively non-convex, the RSS value of the other trial was computed to compare RSS values between trials and determine consistency and reliability of data.

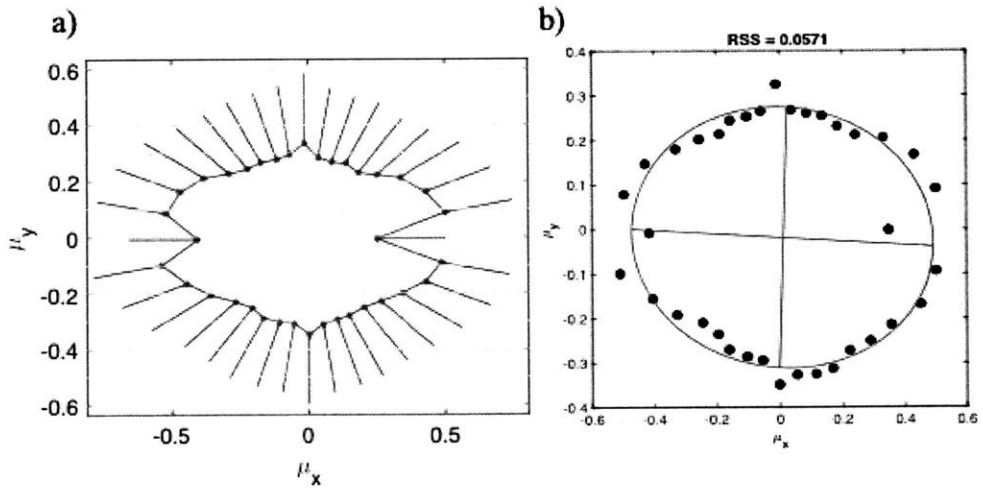

Figure 14: Depicts the method by which the convexity of a limit circle was analyzed. Figure a) shows the original limit curve for a single trial of micro-texture B32. Figure b) shows the best-fit-ellipse in red and the coefficients of friction data as black dots. Residual sum of squares (RSS) was then computed between the experimental data – black dots – and the best-fit-ellipse.

4. Results and Discussion

By experimentally determining the frictional coefficients and plotting the resulting limit curves, the aim was to gain insight into anisotropic friction and determine if it is possible to design anisotropic micro-textures such that unique trajectories can be obtain, i.e. the features of the limit curve are unique and possibly capable of producing unique trajectories. The resulting limit curves are presented below.

4.1 All Material Limit Curves

The limit curves for all three materials are presented using the initial three-by-three sample parameter matrix in Figure 4, and a brief qualitative analysis is presented.

4.1.1 Isotropic Texture

Previous research, [9], has shown that the limit curve of an isotropic surface should be a circle centered around the origin. In order to test that the experimental data obtained from the setup follows theory, a sample with a smooth, isotropic surface was created and tested. The limit curve in Figure 15 was obtained. This curve demonstrates the expected circular shape which is centered about the origin with slip velocities acting normal to the surface. It should be noted that the limit curve below is not perfectly circular, and this is most likely due to imperfect fabrication methods (i.e. defects in the initial molding surface, molding irregularities, etc.). However, the contribution of these errors to the limit curve is slight.

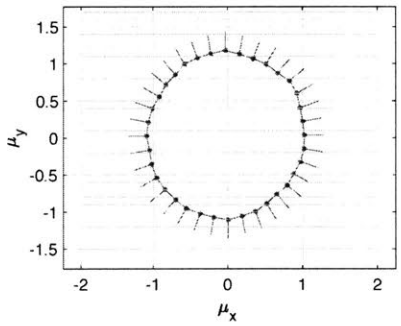

Figure 15: Illustrated is the limit curve for a smooth, isotropic TASK16 sample, without micro-textures. This isotropic limit curve demonstrates an almost circular shape. It was used to compare to anisotropic textures and validate consistency of experimental set-up and result to the literature.

4.1.2 Anisotropic Textures

An initial three-by-three matrix of proposed sample dimensions was created (see Figure 4), and a micro-texture was made for each of the nine proposed micro-textures, a micro-texture for each cell in Figure 4. These d_1 and d_2 parameter values were randomly defined based on the limitations of the photolithography process. Figures 16, 17, and 18 show the resulting limit curve for each of the nine micro-textures for PMC®-770, Smooth-Cast® 61D, and TASK™16 respectively.

From previous research, [9], we expect that an anisotropic micro-texture will result in an elliptical limit curve which most limit curves in Figures 16, 17, and 18 demonstrate. However, within each material there are some uniquely non-convex limit curves.

It should be noted that the limit curves shown below are the result of accounting for and removing the force data from areas that demonstrated wear and clear defects – i.e. non steady state forces were removed if possible. This was done in an attempt to remove any aberrations in the limit curve that were not the result of the micro-textures themselves. However, some limit curves have slight deviation from the expected elliptical shape due to force data that may have slightly spiked during collection and was not removable. Despite these small aberrations in the limit curve it can be inferred that they are elliptical, for example in Figure 17 sample A7.

After removing the non-steady-state force data and ignoring slight aberrations, the limit curves depicted in Figures 16, 17, and 18 are considered valid representations of the micro-texture. Looking holistically at these figures, there appears to be non-convex limit curves within each material type: Figure 16 micro-textures A2 A3, Figure 17 textures A2 A5 A6 A9, Figure 18 textures A2 A3. Interestingly, different materials seem to produce different types of non-convex limit curves.

Prior work also mandates that the slip velocities should be orthogonal to the curve itself based upon the maximum power inequality principle (MPI), this constraint is known as satisfying normality[9]. However, in the limit curves obtained in Figures 16, 17, and 18, a little over half of them do not satisfy normality.

Combining these two observations – lack of normality and non-convex limit curves – it may be the case that the limit curve model under the constraints of MPI are not suited to handle all anisotropic micro-textures, and another model is necessary.

In order to further identify and characterize anisotropic friction, a deeper dive into one of these three materials was taken. TASK™16 – referred to simply as TASK16 - was chosen for further study based on the perceived tunability – symmetric and distinct features - of the non-convex limit curves in its matrix (textures A2 and A3).

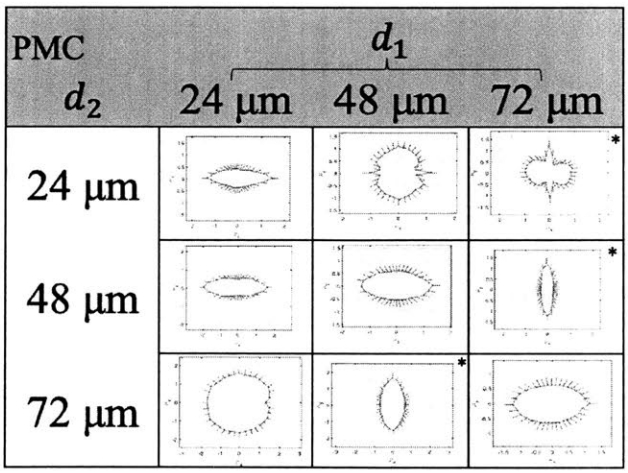

Figure 16: The table portrays the limit curves obtained from the samples made from PMC®-770, labeled simply as PMC above. Those cells with an asterisk had micro-textures oriented horizontally rather than vertically like the rest of the micro-textures. Textures A2 and A3 appear to non-convex. Most of the textures do not demonstrate normality.

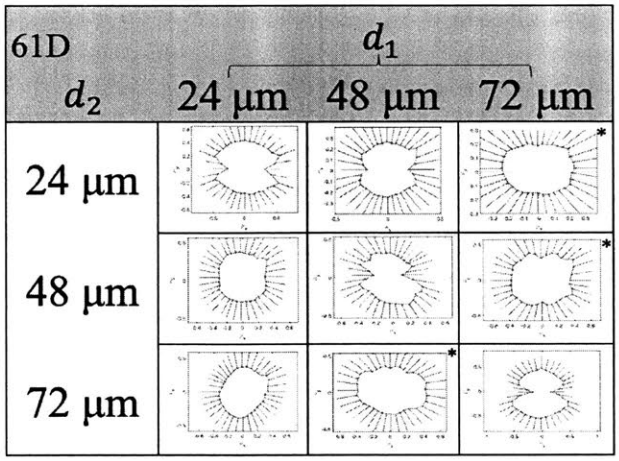

Figure 17: The table portrays the limit curves obtained from the samples made from Smooth-Cast® 61D, labeled above as 61D. Those cells with an asterisk had micro-textures oriented horizontally rather than vertically like the rest of the micro-textures. Textures A1, A2, A5, A6, and A9 appear to be non-convex. Normality is also not upheld by most of the textures.

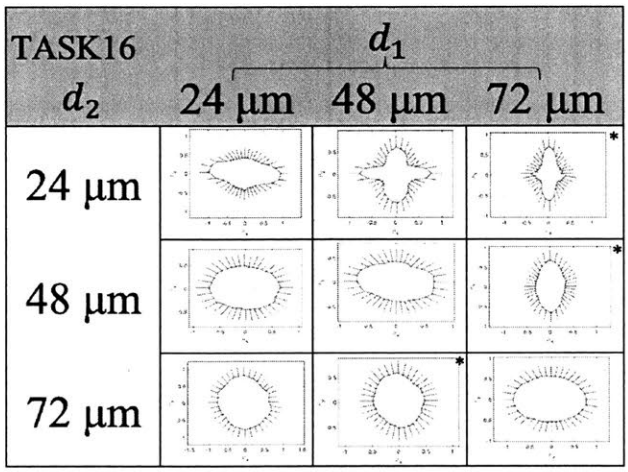

Figure 18: The table portrays the limit curves obtained from the samples made from TASK™16, labeled above as TASK16. Those cells with an asterisk had micro-textures oriented horizontally rather than vertically like the rest of the micro-textures. Textures A2 and A3 are non-convex, and some textures do not demonstrate normality.

4.2 TASK16 Limit Curves

After determining that the TASK16 limit curves appeared the most usefully interesting, the sample parameter matrix was expanded to a six-by-six matrix. See Figure 5. Textures were created and tested for all but one of the sample parameter matrix cells (due to limited resources).

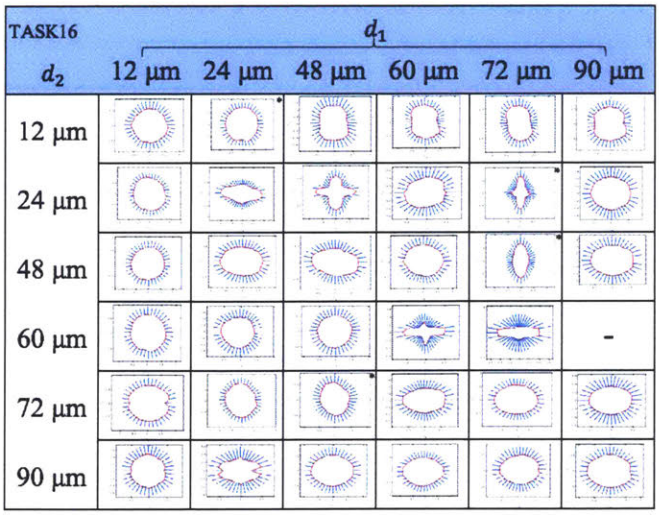

Figure 19: The table portrays the limit curves obtained from the samples made from TASK16 with the additional samples. The empty cell is the result of an unfabricated sample due to limited resources. Those cells with an asterisk had micro-textures oriented horizontally rather than vertically like the rest of the micro-textures. Textures B9, B11, B22, B23, and B32 are non-convex. Only a few textures do not demonstrate normality. It should also be noted that those textures with a d_1 value of 12 appear more isotropic.

4.2.1 Non-convex Limit Curves & RSS

Qualitatively, five limit curves were determined to be non-convex (samples B9, B11, B22, B23, B32). Looking qualitatively at the resulting limit curve for the second trial of these non-convex micro-textures, the irregularity is maintained.

Quantitatively, the limit curve convexity was determined via fitting all the coefficient data to a best-fit-ellipse and then finding the RSS values between that best-fit-ellipse and the data points. Higher RSS values suggest that the data is poorly fit to an ellipse and vice versa. Table 1 shows the RSS values for all micro-textures. Those numbers in parenthesis correspond to the RSS values for another trial that was performed on the same micro-texture.

It can be seen that almost all micro-textures which were qualitatively found to be non-convex were further quantitatively proven to be so as well. Texture B23 has an RSS values that appears more elliptical which is undoubtedly due to the fact that it is essentially elliptical with a slight aberration in the vertical direction which this method of analysis cannot properly capture. Additionally, there does appear to be a slight difference in RSS values between the first and second trial of some micro-textures. This could be due to a slight difference in placement of the sample between each trial or wear/degradation of the surface over time. Regardless, these non-convex limit curve RSS values indicates that the elliptical assumption for anisotropic friction may not be valid for all d_2, d_1 values.

Residual Sum of Squares (RSS)	d_1					
d_2	12 µm	24 µm	48 µm	60 µm	72 µm	90 µm
12 µm	0.0075	0.0147 *	0.0289	0.0505	0.0264	0.0529
24 µm	0.0109	0.039	0.6368. (0.5735)	0.0115	0.0885 * (0.1322)	0.0035
48 µm	0.005	0.0073	0.0097	0.0047	0.0065 *	0.006
60 µm	0.0054	0.0082	0.0059	0.0923 (0.2387)	0.0069 (0.0073)	-
72 µm	0.0509	0.0206	0.0093 *	0.0064	0.0041	0.0019
90 µm	0.0081	0.1043 (0.0571)	0.0048	0.012	0.0055	0.0149

Table 1: A best-fit-ellipse was fit to each of the limit curves in Figure 19 and a residual sum of squares (RSS) was performed between the best-fit-ellipse and the coefficient of friction data. The RSS values are provided above. Those cells with multiple numbers were qualitatively non-convex, and the RSS was determined for both the first and second trial of the micro-texture. Higher values indicate a less elliptical limit curve and vice versa. Those cells with an asterisk had micro-textures oriented horizontally rather than vertically like the rest of the micro-textures. Those cells highlighted in green represented high RSS values and in turn low-convexity.

It is interesting to note that the non-convex limit curves appear to be, for the most part, along the same few d_2 rows. This might suggest that the d_2 value is more important to the anisotropic convexity than the d_1 value. We also see similar types of aberrations, i.e. those that look like plus signs and those that look like ellipses with slight spikes, are along the same $d_2 = 24$ row. This suggest the possibility of designing frictional limit curves of a specific type based on the micro-texture parameters.

One sample in particular (B11) is highly promising as a useful and designable limit curve. It demonstrates a symmetric and plus-sign-like shape that could be seen as composed of two elliptical limit curves superimposed together. This could give the user the ability to "flip" their frictional contact force with a single texture.

As another observation, one would expect that those micro-textures with the same d_1 and d_2 values - those resembling a square wave - would have a similar limit curve, however there is a distinctive difference as one moves along the diagonal of the matrix. A Fast Fourier Transform was performed and ruled out resonance throughout the micro-texture as a causal effect. The exact cause of this changing limit curve along the diagonal is of interest in further study. Additionally, those micro-textures along the first column exhibit nearly isotropic micro-textures, and those toward the center of the matrix seems to have more "interesting" limit curves. Finally, the limit curves in Figure 19 disagree with the literature in that the coefficients of friction across the grooves – valleys and canyons – are lower than those along the grooves. A disparity exists between the frictional force pattern from the micro-sized textures in the study and the macro-sized features utilized in previous studies [11]. In total, these anisotropic observations are very promising for the goal of controlled friction.

5. Conclusion

Convexity is an important property of a limit curve for avoiding ambiguity when MPI is assumed. The convexity of various anisotropic micro-textures was determined both qualitatively and quantitatively, and a qualitative analysis of normality was conducted to better understand anisotropic friction. A lack of normality and convexity were discovered which violates MPI. Interesting anisotropic friction behavior was observed which suggests the possibility of designing anisotropic friction to guarantee the convergence of motion and remove uncertainty in frictional contact forces. A new model – abandoning limit curves and MPI – should be pursued.

An initial examination of a few micro-textures across three different materials was made and qualitatively non-convex limit curves were found for all three different materials. A single material was chosen from the three, and more micro-textures with further parameters were tested.

Within that single material, TASK16, five limit curves were found to be convex qualitatively and four of these were validated quantitatively via RSS values between a best-fit-ellipse and the data. There appears to be some pattern between the type of aberration and its d_2 parameter size or width of the valley. High RSS values, indicating non-convexity, were seen to be about 0.6 to 0.08. Of these non-convex limit curves there exists one in particular which demonstrates promise in controlling contact interaction via micro-texture (B11).

In future work, a deeper exploration of the relationship between the parameter size, particularly d_2 and square wave parameters should be made to more clearly understand how to design appropriately non-convex limit curves. Additionally, this paper did not have the resources to explore the relationship between different materials and different limit curves in depth, but an analysis of the effects of material would be useful. Finally, in the future a model will be created to characterize the non-convex limit curves produced. The model would serve as a map between frictional coefficients and micro-texture parameters. This model will be used to then design a frictional surface capable of controlling trajectories which is useful for designing friction and in turn the frictional interaction between surfaces. Such technology could remove uncertainty and give roboticist more control over the interactions that their robots have with the environment, particularly in the fields of locomotion and manipulation.

Note that the dataset used in this research endeavor is available to other researchers interested in friction behavior caused by micro-textures on the MCube Lab website (http://mcube.mit.edu/datasets/anisotropic.html).

6. Bibliography

[1] Feng, Z.-Q., Hjiaj, M., de Saxcé, G., and Mróz, Z., 2006, "Influence of Frictional Anisotropy on Contacting Surfaces during Loading/Unloading Cycles," International Journal of Non-Linear Mechanics, **41**(8), pp. 936–948.

[2] Ma, D., and Rodriguez, A., 2018, "Friction Variability in Planar Pushing Data: Anisotropic Friction and Data-Collection Bias," IEEE Robotics and Automation Letters, **3**(4), pp. 3232–3239.

[3] Bauza, M., and Rodriguez, A., 2017, "A Probabilistic Data-Driven Model for Planar Pushing," *2017 IEEE International Conference on Robotics and Automation (ICRA)*, pp. 3008–3015.

[4] Subramani, G., and Zinn, M. R., 2015, "Tackling Friction - an Analytical Modeling Approach to Understanding Friction in Single Tendon Driven Continuum Manipulators," *2015 IEEE International Conference on Robotics and Automation (ICRA)*, IEEE, Seattle, WA, USA, pp. 610–617.

[5] Mróz, Z., and Stupkiewicz, S., 1994, "An Anisotropic Friction and Wear Model," International Journal of Solids and Structures, **31**(8), pp. 1113–1131.

[6] Baum, M., Kovalev, A., Michels, J., and Gorb, S., 2014, "Anisotropic Friction of the Ventral Scales in the Snake Lampropeltis Getula Californiae," Tribology Letters, **54**.

[7] Zmitrowicz, A., 1999, "An Equation of Anisotropic Friction with Sliding Path Curvature Effects," International Journal of Solids and Structures, **36**(19), pp. 2825–2848.

[8] Michalowski, R., and Mroz, Z., 1978, "Associated and Non-Associated Sliding Rules in Constant Friction Problems," Archives of Mechanics, **30**(3), pp. 259–276.

[9] Goyal, S., Ruina, A., and Papadopoulos, J., 1991, "Planar Sliding with Dry Friction Part 1. Limit Surface and Moment Function," Wear, **143**(2), pp. 307–330.

[10] Mróz, Z., Kucharski, S., and Páczelt, I., 2018, "Anisotropic Friction and Wear Rules with Account for Contact State Evolution," Wear, **396–397**, pp. 1–11.

[11] Konyukhov, A., Vielsack, P., and Schweizerhof, K., 2008, "On Coupled Models of Anisotropic Contact Surfaces and Their Experimental Validation," Wear, **264**(7), pp. 579–588.

[12] Maegawa, S., Itoigawa, F., and Nakamura, T., 2016, "Effect of Surface Grooves on Kinetic Friction of a Rubber Slider," Tribology International, **102**, pp. 326–332.